

# Design and Implementation of CLLC Bidirectional Converter with Wide Voltage Range on Low Side

Jie Li  
Department of Electrical  
Engineering,  
National Cheng-Kung  
University  
Tainan, Taiwan  
[ve6092119@gs.ncku.edu.tw](mailto:ve6092119@gs.ncku.edu.tw)

Wen-Hsuan Lee  
Department of Electrical  
Engineering,  
National Cheng-Kung  
University  
Tainan, Taiwan  
[ve6112090@gs.ncku.edu.tw](mailto:ve6112090@gs.ncku.edu.tw)

Jiann-Fuh Chen  
Department of Electrical  
Engineering,  
National Cheng-Kung  
University  
Tainan, Taiwan  
[chenjf@mail.ncku.edu.tw](mailto:chenjf@mail.ncku.edu.tw)

Tsorn-Juu Liang  
Department of Electrical  
Engineering,  
National Cheng-Kung  
University  
Tainan, Taiwan  
[tjliang@mail.ncku.edu.tw](mailto:tjliang@mail.ncku.edu.tw)

**Abstract**—The design and implementation of a high-frequency isolated bidirectional resonant converter for efficient energy transfer between the DC bus and the batteries in electric cars are the focal points of this research. To achieve high switching frequency, the converter utilizes a planar transformer and wide bandgap elements. The main circuit comprises a three-level half-bridge structure on the high voltage side, a full bridge structure on the low voltage side, and a CLLC resonant tank. The circuit control can be simplified by the symmetrical resonant tank of circuit characteristics of bidirectional power flow. This converter enables soft switching, effectively reducing switching losses. The research also includes the derivation of voltage-gain curves, steady-state equivalent models, and an analysis of the operating principles of the bidirectional resonant converter. For energy conversion control, the research employs the DSP TMS320F28379D with a rated power of 1 kW, a DC bus voltage of 800 V, and battery voltages ranging from 200 V and 400 V. The converter achieves a maximum efficiency of 94.2%.

**Keywords**—Bidirectional DC-DC converters, planar transformer, wide bandgap semiconductor, zero voltage switching, zero current switching.

## I. INTRODUCTION

Bidirectional DC-DC converters (BDCs) are the important interface in energy storage systems to stabilize the power conditions of high voltage bus (utility power) and low voltage bus (battery) as shown Fig. 1(a) [1], [2].

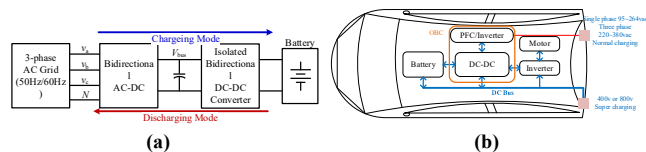


Fig. 1. (a) General bidirectional charging system, (b) The structure of the EV.

In recent years, automobiles have moved towards the development of hybrid and electric modes, and electric vehicles are facing strong market demand. These vehicles offer the potential for improved energy utilization, while also presenting opportunities to decrease petroleum consumption, mitigate air pollution, and reduce noise levels. However,

challenges still exist for these vehicles, including a limited cruising range, inadequate battery charging infrastructure, and extended battery charging time. As a result, the progress in electric vehicle (EV) battery charger development is steadily increasing. The EV structure is shown in Fig. 1(b) [3]-[6].

EV battery chargers can be categorized based on power flow as either on-board or off-board chargers, supporting either unidirectional or bidirectional power flow. According to different requirements of the battery charging time and the various types of EVs, three charging levels of EV battery chargers are defined. A comparison of EV charging levels is listed in TABLE I [7], [8]. The major differences between level 1 and 2 are that level 2 charging can use single phase or three phase AC input. Level 3 chargers convert AC to DC within a charging station. The DC power directly from charging station into EV's batteries. The level 3 charging's with large converters big like more room to house. However, level 1 charger works well on PHEVs. And some of the level 2 battery chargers are designed for off-board.

TABLE I. COMPARISON OF EV CHARGER [7], [8].

	Level 1	Level 2	Level 3
Input source	single-phase AC	single or three-phase AC	three-phase AC
Output current type	AC	AC	DC
Charging location	Single house Apartment	Retail and Hospitality Business Workplace	Parking Lot Service Station
Charger type	On-board	On-board/Off-board	Off-board
Power level	1~5 kW	5~50 kW	50 kW~350 kW
Charging time	8~14 hours	3~8 hours	15~30 minutes

The paper is divided into five sections. Section II focuses on the analysis and design of the operating modes of the CLLC bidirectional DC-DC converter. Section III covers the steady-state analysis and component design. In Section IV, the obtained simulation and experimental results of the CLLC

bidirectional converter are presented. Finally, Section V provides the conclusion of the paper.

## II. OPERATING PRINCIPLE

The chosen circuit for EV charger applications is the three-level bidirectional CLLC resonant converter circuit, as illustrated in Fig. 2. This particular topology incorporates a three-level neutral point clamped (NPC) half-bridge structure, which effectively addresses the issue of semiconductor rated voltage. The battery side of the converter utilizes a full bridge structure. The CLLC resonant tank facilitates seamless power transfer in both directions, making it possible to achieve bidirectional power flow. As a result, the converter exhibits an asymmetric configuration. The characteristics of this topology resemble those of a conventional LLC resonant converter. However, it incorporates additional resonant components on the secondary side. The resonant tank is formed by  $L_{r1}$ ,  $L_{r2}$ ,  $L_m$ ,  $C_{r1}$ , and  $C_{r2}$ . In addition, a dual function is served by the capacitors  $C_{r1}$  and  $C_{r2}$  as both the resonant capacitors and the blocking capacitors to prevent flux imbalance in the transformer.

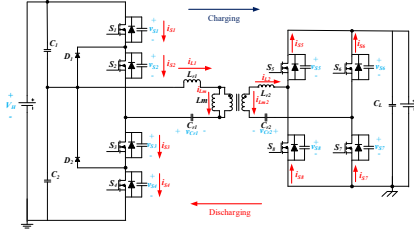


Fig. 2. Bidirectional DC-DC CLLC resonant converter

The operation principles, equivalent models, characteristics of voltage gain, and parameter design are discussed in this section. In order to simplify the analysis of the CLLC resonant converter, certain assumptions need to be made:

- The converter operates under steady-state conditions.
- The GaN-MOSFETs switches  $S_1$ ,  $S_2$ ,  $S_3$ ,  $S_4$ ,  $S_5$ ,  $S_6$ ,  $S_7$ , and  $S_8$  can be used to conduct reverse current and parasitic capacitance are considered.
- The capacitance  $C_1$ ,  $C_2$ , and  $C_L$  are sufficiently large enough to keep the voltage constant. The value of inductor  $L_{r1}$  is less than that of inductor  $L_{r2}$ .
- Inductors and capacitors are ideal.

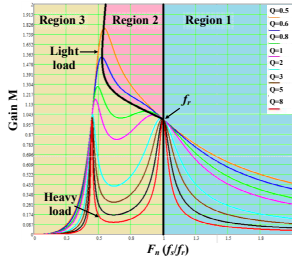


Fig. 3. Voltage-gain curves of CLLC resonant converter.

Fig. 3 [9] depicts the categorization of the operation of a bidirectional resonant converter into three regions. At the series

resonant frequency  $f_r$ , this topology maintains a constant gain. As a result of the CLLC-type resonant tank, this converter exhibits three resonant frequencies. Under heavy load conditions, the voltage-gain curves display two peaks. The operation of the converter within regions 1 and 2 ensures that the inductive impedance of the resonant tank is maintained.

### A. Charging Mode (Region 2)

The definitions of voltage and current direction in the charging mode is shown in Fig. 3 [9]. The converter is operated below resonant frequency. Operating with this condition, the primary side switches also can achieve zero voltage switching (ZVS) turned on. Moreover, the switches on secondary side can achieve zero current switching (ZCS) turned off which can reduce switching loss. On the other hand, the RMS current became higher produced more conduction loss. Fig. 4 depicts the key waveform, while Fig. 5 illustrates the current flow path.

#### Mode I [ $t_0$ , $t_1$ ]:

Starting at  $t = t_0$ ,  $S_1$  and  $S_2$  are simultaneously activated using the ZVS technique. Capacitors  $C_{r1}$  and  $C_{r2}$  resonate with inductor  $L_{r1}$ , reducing  $i_{Lm}$  and  $i_{Lr1}$ . However,  $i_{Lr1}$  does not match  $i_{Lm}$ .  $V_H$  powers  $V_{Bat}$ , charging  $C_L$  and  $V_{Bat}$ .  $S_6$  and  $S_8$  act as synchronous rectifiers. This mode persists until  $i_{Lr1}$  aligns with  $i_{Lm}$ , signifying its completion.

#### Mode II [ $t_1$ , $t_2$ ]:

In this mode, the currents  $i_{Lr1}$  and  $i_{Lm}$  are aligned by simultaneously turning on switches  $S_1$  and  $S_2$ . Resonance between inductor  $L_m$ , capacitors  $C_{r1}$  and  $C_{r2}$ , and inductor  $L_{r1}$  increases the resonant current  $i_{Lr1}$ . Switches  $S_6$  and  $S_8$  are then turned off using the ZCS technique to achieve transformer decoupling.  $C_L$  charges  $V_{Bat}$  during this process. The mode concludes upon switching off  $S_1$ .

#### Mode III [ $t_2$ , $t_3$ ]:

$S_2$  remains on while  $S_1$  is off in the  $t = t_2$  mode. Current  $i_{Lr1}$  flows through  $S_2$ ,  $D_1$ ,  $L_m$ ,  $L_{r1}$ , and  $C_{r1}$ .  $D_1$  is turned on, resulting in the clamping of  $S_1$  by  $C_1$ . The parasitic capacitance  $C_{S1}$  charges and reaches half of  $V_H$ .  $C_{S3}$  and  $C_{S4}$  discharge, decreasing to one-fourth of  $V_H$  each. The transformer remains decoupled, and  $V_{Bat}$  continues to charge with  $C_L$ . The mode comes to a conclusion when switch  $S_2$  is turned off.

#### Mode IV [ $t_3$ , $t_4$ ]:

When  $S_2$  is powered off at  $t = t_3$ , the voltage across  $S_1$  is reduced to half of  $V_H$ . The charging of the parasitic capacitance  $C_{S1}$  comes to a halt at this point, while the parasitic capacitors  $C_{S3}$  and  $C_{S4}$  continue to discharge. In this mode, the voltage across  $S_3$  and  $S_4$  gradually decreases from one-fourth of  $V_H$  to zero. Simultaneously, the parasitic capacitance  $C_{S2}$  charges up, resulting in  $V_{S2}$  reaching half of  $V_H$ . This mode concludes when the current through  $D_1$  ceases to flow and  $V_{S2}$  reaches half of  $V_H$ .

#### Mode V [ $t_4$ , $t_5$ ]:

All power MOSFETs are switched off at  $t = t_4$ . The body diodes of  $S_3$  and  $S_4$  allow the resonant current  $i_{Lr1}$  to flow

through them. The magnetizing inductance  $L_m$  releases energy to  $C_L$  and  $V_{Bat}$ . The resonant current  $i_{Lr1}$  flows through the parasitic diode of  $S_5$  and  $S_7$ . ZVS is enabled when the operation reaches stages  $S_3$  and  $S_4$  in this mode.

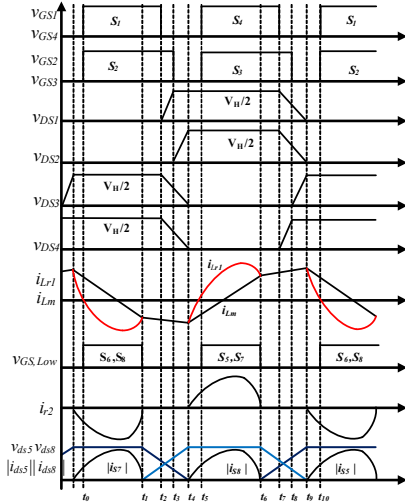


Fig. 4. Key waveforms of the circuit in step down mode (Region 2)

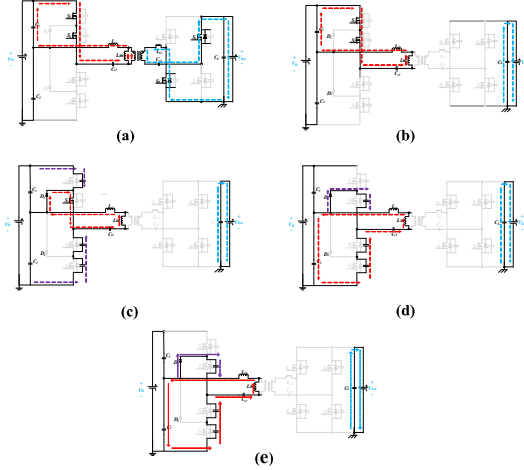


Fig. 5. Operation of the converter in charging mode (Region 2) : (a) mode I  $[t_0, t_1]$ , (b) mode II  $[t_1, t_2]$ , (c) mode III  $[t_2, t_3]$ , (d) mode IV  $[t_3, t_4]$ , and (e) mode V  $[t_4, t_5]$ .

### B. Charging Mode (Region 1)

Fig. 6 and Fig. 7 showcase the illustrations of the key waveforms and current flow path of the CLLC resonant converter. The converter operates above the resonant frequency. During turn-on, ZVS can still be achieved by the primary side switches. However, ZCS is not achieved by the switches on the secondary side during turn-off. The modes from  $t_5$  to  $t_{10}$  are symmetrical to those of the previous half cycle and are therefore omitted in this section.

#### Mode I $[t_0, t_1]$ :

This mode commences at  $t = t_0$  when both  $S_1$  and  $S_2$  are turned on using ZVS, and the parasitic diodes of  $S_5$  and  $S_7$  conduct. The magnetizing inductor  $S_5$  and  $S_7$  provides energy

to the high-voltage side  $V_H$ , while  $L_{r1}$  delivers energy to  $C_L$  and the load  $V_{Bat}$ .

#### Mode II $[t_1, t_2]$ :

$S_1$  and  $S_2$  are still simultaneously on, while  $S_6$  and  $S_8$  function as synchronous rectifiers. When  $t = t_1$ , the high side voltage  $V_H$  causes the slope of  $i_{Lr1}$  and  $i_{Lm}$  to change from negative to positive. The magnetizing inductor does not participate in resonance, leading to a gradual increase in  $i_{Lm}$ . The mode concludes when  $i_{Lm}$  reaches zero.

#### Mode III $[t_2, t_3]$ :

$S_1$  has been shut down at  $t = t_2$ . Consequently, the resonant current flows through  $D_1$ ,  $S_2$ ,  $C_{r1}$ ,  $L_{r1}$  and  $L_m$ . The parasitic capacitance of  $S_1$  is charged, while the voltage across  $S_1$  is clamped by capacitor  $C_1$ , causing  $C_{S1}$  to charge up to half of  $V_H$ . The output energy is provided by the magnetizing inductor. This mode concludes when  $S_2$  is switched off.

#### Mode IV $[t_3, t_4]$ :

While  $S_2$  is switched off at  $t = t_3$ , the voltage across  $S_1$  measures half of  $V_H$ . At the same time, the charging of the parasitic capacitance  $C_{S1}$  ceases. Simultaneously, the parasitic capacitors  $C_{S3}$  and  $C_{S4}$  continue to discharge. In this operating mode, the voltage across switches  $S_3$  and  $S_4$  progressively reduces from one-quarter of  $V_H$  to zero. The parasitic capacitance  $C_{S2}$  is charged, resulting in the voltage  $V_{S2}$  reaching half of  $V_H$ . The output energy is provided by the magnetizing inductor. This mode concludes when the current stops flowing through  $D_1$ , and the voltage  $V_{S2}$  reaches half of  $V_H$ .

#### Mode V $[t_4, t_5]$ :

All switches are in the off position at  $t = t_4$ . The resonant current  $i_{Lr1}$  is conducted through the body diodes of  $S_3$  and  $S_4$ , while the magnetizing inductance  $L_m$  supplies energy to  $V_{Bat}$ . At the same time, the resonant current  $i_{Lr2}$  flows through the parasitic diodes of  $S_5$  and  $S_7$ . The mode concludes when switches  $S_3$  and  $S_4$  achieve ZVS during turn-on.

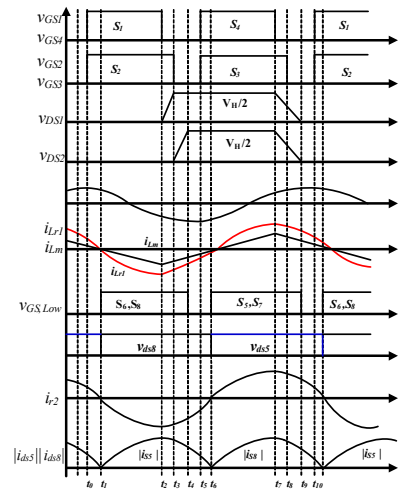


Fig. 6. Key waveforms of the circuit in step down mode (Region 1)

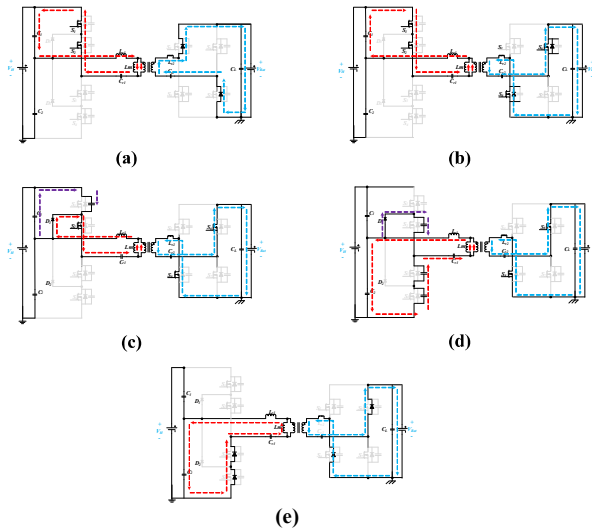


Fig. 7. Operation of the converter in charging mode (Region 1) : (a) mode I[ $t_0, t_1$ ], (b) mode II[ $t_1, t_2$ ], (c) mode III[ $t_2, t_3$ ], (d) mode IV[ $t_3, t_4$ ], and (e) mode V[ $t_4, t_5$ ].

### C. Discharging Mode

The key waveform of the CLLLC resonant converter is illustrated in Fig. 8. Fig. 9 illustrates the current flow path. The converter operates below the resonant frequency, enabling the full bridge side switches to achieve ZVS during turn-on. Meanwhile, the switches on the three-level half bridge side achieve ZCS during turn-off. The operating modes from  $t_5$  to  $t_8$  are symmetrical to those of the previous half cycle, and thus, the analysis of these modes is omitted in this section.

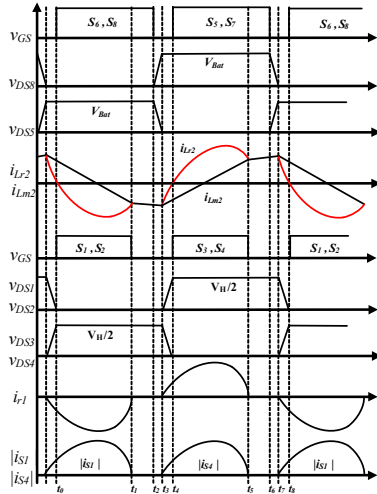


Fig. 8. Key waveforms of the circuit in step up mode

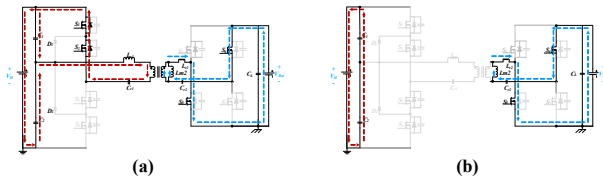


Fig. 9. Operation of the converter in charging mode (Region 1) : (a) mode I[ $t_0, t_1$ ], (b) mode II[ $t_1, t_2$ ], (c) mode III[ $t_2, t_3$ ], and (d) mode IV[ $t_3, t_4$ ].

### Mode I [ $t_0, t_1$ ]:

Initially,  $S_6$  and  $S_8$  are turned on at  $t = t_0$ . The resonant process involves the participation of resonant capacitors  $C_{r1}$ ,  $C_{r2}$ , and resonant inductance  $L_{r2}$ . Consequently, the currents  $i_{Lm2}$  and  $i_{Lr2}$  decrease. Energy flows from the battery voltage side to the high voltage side, charging capacitor  $C_1$  and the load  $V_H$ . The mode ends when the currents  $i_{Lr2}$  and  $i_{Lm2}$  balance each other.

### Mode II [ $t_1, t_2$ ]:

$S_6$  and  $S_8$  remain turned on during  $t = t_1$ . The ZCS turn-off of  $S_1$  and  $S_2$  takes place. The resonant current  $i_{Lr2}$  becomes equal to  $i_{Lm2}$ . The transformer is decoupled, preventing the transfer of energy from the DC bus side to the high-voltage side. The magnetizing inductor actively participates in the resonance process, with  $V_H$  continuously supplying energy to  $L_{r2}$  and  $L_m$ . Consequently, the resonant current  $i_{Lr2}$  gradually increases. The load  $V_H$  receives energy from capacitors  $C_1$  and  $C_2$ . This mode comes to an end when  $S_6$  and  $S_8$  are switched off.

### Mode III [ $t_2, t_3$ ]:

The power to  $S_6$  and  $S_8$  is cut off at  $t = t_2$ . The resonant current  $i_{r2}$  charges the parasitic capacitors of  $S_6$  and  $S_8$ , while discharging the capacitors of switches  $S_5$  and  $S_7$ . This results in an increase in the voltage across capacitors  $C_{S6}$  and  $C_{S8}$  to  $V_{Bat}$ , while the voltage across  $C_{S5}$  and  $C_{S7}$  decreases to zero. The transformer remains decoupled, and energy is supplied to  $V_H$  from  $C_1$  and  $C_2$ . This mode concludes when the current  $i_{Lm2}$  is no longer equal to  $i_{Lr2}$ .

### Mode IV [ $t_3, t_4$ ]:

All GaN-MOSFETs switch off at  $t = t_3$ . The resonance process involves the engagement of the resonant capacitors  $C_{r1}$  and  $C_{r2}$ , in conjunction with the participation of the resonant inductor  $L_r$ . In the positive direction, the current  $i_{Lm2}$  decreases, and energy is discharged from the magnetizing inductor  $L_{m2}$  to the high-voltage side. During resonance, the current  $i_{r1}$  charges capacitors  $C_{S1}$  and  $C_{S2}$ , while simultaneously discharging capacitors  $C_{S3}$  and  $C_{S4}$ . The resonant current  $i_{Lr1}$  starts flowing through the body diodes of  $S_3$  and  $S_4$  when the voltage across  $S_1$  and  $S_2$  reaches half of  $V_H$ , respectively, and the voltage across  $S_3$  and  $S_4$  decreases to zero, respectively. The mode concludes when switches  $S_3$ ,  $S_4$ ,  $S_5$ , and  $S_7$  achieve ZVS during the turn-on process.

## III. STYLING STEADY-STATE ANALYSIS OF PROPOSED CONVERTER

The steady-state models, obtained through the use of the fundamental harmonic approximation (FHA) approach, are

depicted in Fig. 10. These models consider all the resonant components referred to the same side of the transformer. The structures of the resonant tank in the charging stage and discharging stage exhibit symmetry, but the values of equivalent circuit components differ. This leads to distinct voltage-gain characteristics in each direction.

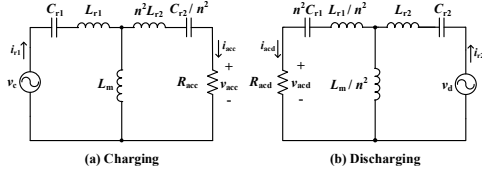


Fig. 10. FHA models of the bidirectional CLLC resonant converter

The discussion later is classified into charging mode and discharging mode. The charging mode equivalent circuit of CLLC is shown in Fig. 11 (a). Since evaluating the resonant tank's steady state requires extensive calculation. To simplify the analysis, FHA is used. The output voltage  $v_{acc}$ 's FHA is presented as equation (1). The root-mean-square value of  $v_{acc}$  is presented as equation (2).

$$v_{acc,FHA}(t) = \frac{4n \cdot V_L}{\pi} \sin(2\pi f_s t) \quad (1)$$

$$v_{acc,rms} = \frac{2\sqrt{2}n \cdot V_L}{\pi} \quad (2)$$

The output current  $i_{acc}$  is similar to sinusoidal wave. It can be referred from the average output current  $I_L$ , which is expressed as equation (3), where the  $i_{acc,pk}$  is the peak value of  $i_{acc}$ . The root-mean square value of  $i_{acc}$  is presented as equation (4).

$$I_L = \frac{1}{\pi} \int_0^\pi n \cdot i_{acc,pk} \sin(\omega t) d\omega t = \frac{2ni_{acc,pk}}{\pi} \quad (3)$$

$$i_{acc,rms} = \frac{i_{acc,pk}}{\sqrt{2}} = \frac{\pi \cdot I_L}{2\sqrt{2} \cdot n} \quad (4)$$

According to equations (1) and (2), the equivalent load  $R_{acc}$  is expressed as equation (5), where  $R_L$  is the dc load  $V_{Bat}/I_L$ .

$$R_{acc} = \frac{v_{acc,rms}}{i_{acc,rms}} = \frac{8}{\pi^2} \left(\frac{N_p}{N_s}\right)^2 R_L \quad (5)$$

The equivalent circuit of charging mode is similar to discharging mode. The equivalent circuit of discharging mode is shown in Fig. 11 (b). In this mode, the output voltage  $v_{acd}$ 's FHA is presented as equation (6). The root-mean-square value of  $v_{acd}$  is presented as equation (7).

$$v_{acd,FHA}(t) = \frac{2 \cdot V_H}{n \cdot \pi} \sin(2\pi f_s t) \quad (6)$$

$$v_{acd,rms} = \frac{\sqrt{2} \cdot V_H}{n \cdot \pi} \quad (7)$$

The output current  $i_{acd}$  is similar to sinusoidal wave. It can be referred from the average output current  $I_H$ , which is expressed as equation (8), where the  $i_{acd,pk}$  is the peak value of  $i_{acd}$ . The root-mean-square value of  $i_{acd}$  is presented as equation (9).

$$I_H = \frac{1}{2\pi} \int_0^{2\pi} \frac{1}{n} \cdot i_{acd,pk} \sin(\omega t) d\omega t = \frac{i_{acd,pk}}{n\pi} \quad (8)$$

$$i_{acd,rms} = \frac{i_{acd,pk}}{\sqrt{2}} = \frac{n \cdot \pi \cdot I_H}{\sqrt{2}} \quad (9)$$

According to equations (8) and (9), the equivalent load  $R_{acd}$  is expressed as equation (10), where  $R_H$  is the dc load  $V_H/I_H$ .

$$R_{acd} = \frac{v_{acd,rms}}{i_{acd,rms}} = \frac{2}{\pi^2} \left(\frac{N_s}{N_p}\right)^2 R_H \quad (10)$$

The voltage conversion ratio of the equivalent circuit can be derived by the impedance division. The charging and discharging mode voltage conversion ratio are presented as equations (11) and (12).

$$M_f = \left| \frac{v_{acc}}{v_c} \right| = \left| \frac{Z_{Lm} \parallel (Z'_{Lr2} + Z'_{Cr2} + R_{acc})}{Z_{Lr1} + Z_{Cr1} + [Z_{Lm} \parallel (Z'_{Lr2} + Z'_{Cr2} + R_{acc})]} \times \frac{R_{acc}}{Z'_{Lr2} + Z'_{Cr2} + R_{acc}} \right| \quad (11)$$

$$M_b = \left| \frac{v_{acd}}{v_d} \right| = \left| \frac{[Z'_{Lm} \parallel (Z'_{Lr1} + Z'_{Cr1} + R_{acd})]}{Z_{Lr2} + Z_{Cr2} + [Z'_{Lm} \parallel (Z'_{Lr1} + Z'_{Cr1} + R_{acd})]} \times \frac{R_{acd}}{Z'_{Lr1} + Z'_{Cr1} + R_{acd}} \right| \quad (12)$$

where

$$\begin{aligned} \omega_s &= 2\pi f_s, Z_{Lm} = j\omega_s L_m, Z'_{Lm} = j\omega_s L_m / n^2, Z_{Lr1} = j\omega_s L_{r1}, Z'_{Lr1} = j\omega_s L_{r1} / n^2, \\ Z_{Lr2} &= j\omega_s L_{r2}, Z'_{Lr2} = j\omega_s n^2 L_{r2}, Z_{Cr1} = 1/j\omega_s C_{r1}, Z'_{Cr1} = 1/j\omega_s n^2 C_{r1}, \\ Z_{Cr2} &= 1/j\omega_s C_{r2}, Z'_{Cr2} = n^2 / j\omega_s C_{r2}. \end{aligned}$$

In order to simplify the voltage conversion  $M_f$ ,  $M_b$ , and design procedure, certain assumptions are defined as depicted in the following equations. The normalized frequency is the ratio of operating frequency and resonant frequency. The normalized frequency of charging mode  $f_{n_f}$  and discharging mode  $f_{n_b}$  are expressed as equations (13) and (14).  $f_{r_f}$  and  $f_{r_b}$  stand for resonant frequency.

$$f_{n_f} = \frac{f_s}{f_{r_f}} = \frac{f_s}{\frac{1}{2\pi\sqrt{L_{r1}C_{r1}}}} \quad (13)$$

$$f_{n_b} = \frac{f_s}{f_{r_b}} = \frac{f_s}{\frac{1}{2\pi\sqrt{L_{r2}C_{r2}}}} \quad (14)$$

The quality factor in charging and discharging mode are defined as equation (15) and (16).

$$Q_f = \frac{\sqrt{L_{r1}/C_{r1}}}{R_{acc}} \quad (15)$$

$$Q_b = \frac{\sqrt{L_{r2}/C_{r2}}}{R_{acd}} \quad (16)$$

The inductance ratio  $k$  is expressed as equation (17). The capacitance ratio  $m$  is defined as the ratio between high-voltage side resonant capacitance and battery side resonant capacitance that refer to the high-voltage side.  $m$  is expressed as equation (18).

$$k = \frac{L_m}{L_{r1}} \quad (17)$$

$$m = \frac{C_{r2}}{C_{r1}} \left( \frac{N_s}{N_p} \right)^2 \quad (18)$$

With the equations (13) to (18), the voltage conversion ratio  $M_f$  and  $M_b$  can be simplified to equations (19) and (20)

$$M_f = \frac{k}{\left| \frac{Q_f}{m} [-m(2k+1)f_{n,f} + (k+1)(m+1)f_{n,f}^{-1} - f_{n,f}^{-3}] + j(k+1-f_{n,f}^{-2}) \right|} \quad (19)$$

$$M_b = \frac{k}{|Q_b[-(2k+1)f_{n,b} + (k+1)(m+1)f_{n,b}^{-1} - mf_{n,b}^{-3}] + j(k+1-f_{n,b}^{-2})|} \quad (20)$$

With different operating frequency, the gain curve can be drawn by the equations (19) and (20). Though the design of  $Q$ ,  $k$  and  $m$ 's value, the converter can meet the demands.

In charging mode, since the dead time of the circuit is very short, the peak value of magnetizing inductor current  $I_{Lm,pk}$  can be expressed as equation (21). The duty cycle  $D$  is 48%. The waveform of magnetizing inductor current is similar to triangle wave, the root mean square value of current is approximated as equations (22).

$$I_{Lm,pk} = \frac{V_{Lm}}{L_m} \frac{D}{2f_s} = \frac{V_{Lm}}{4f_s L_m} \quad (21)$$

$$I_{Lm,rms} = \frac{I_{Lm,pk} c}{\sqrt{3}} = \frac{V_{Lm}}{4\sqrt{3}f_s L_m} \quad (22)$$

The root-mean-square value of battery side resonant current  $i_{acc,rms}$  is same as equation (4). The root mean square value of high-voltage side resonant current  $I_{Lr1,rms}$  includes the magnetizing inductor current and battery side resonant current referred to high-voltage side.  $I_{Lr1,rms}$  is expressed as equation (23).

$$I_{Lr1,rms} = \sqrt{I_{Lm,rms}^2 + i_{acc,rms}^2} = \sqrt{\frac{V_{Lm}^2}{48f_s^2 L_m^2} + \frac{\pi^2 I_L^2}{8n^2}} \quad (23)$$

The root-mean-square value of the current  $I_{sw,rms\_h}$  which flow through switches at high-voltage side. Because the three level half bridge structure, only about half cycle of the resonant current can flow through. Hence  $I_{sw,rms\_h}$  is equal to

$I_{L1,rms}$  divided by square root of two.  $I_{sw,rms\_h}$  is expressed as equation (24).

$$I_{sw,rms\_h} = \sqrt{\frac{V_{Lm}^2}{96f_s^2 L_m^2} + \frac{\pi^2 I_L^2}{16n^2}} \quad (24)$$

With the similar situation, the current only flow through battery side switches during half period.  $I_{DL,rms}$  is equal to  $i_{acc,rms}$  divided by square root of two. Hence, equation (25) represents the root-mean-square value of the current flowing through the switches at the battery side.

$$I_{DL,rms} = \frac{\pi}{4} I_L \quad (25)$$

Equation (26) presents the peak voltage across the resonant capacitor at the high-voltage side, considering that the resonant current resembles a sine wave.

$$V_{Cr1,pk} = \frac{\sqrt{2}I_{Lr1,rms}}{\omega C_{r1}} = \frac{\sqrt{\frac{V_{Lm}^2}{24f_s^2 L_m^2} + \frac{\pi^2 I_L^2}{4n^2}}}{2\pi f_s C_{r1}} \quad (26)$$

In discharging mode, the calculations are similar to charging mode. The root-mean-square value of battery side resonant current  $I_{r2,rms}$  includes the magnetizing inductor current and high-voltage side resonant current referred to battery side.  $I_{r2,rms}$  is expressed as equation (27).

In discharging mode, the calculations are similar to charging mode. The root-mean-square value of battery side resonant current  $I_{r2,rms}$  includes the magnetizing inductor current and high-voltage side resonant current referred to battery side.  $I_{r2,rms}$  is expressed as equation (27).

$$I_{Lr2,rms} = \sqrt{(n \cdot I_{Lm,rms})^2 + I_{acd,rms}^2} = \sqrt{\frac{n^2 V_{Lm}^2}{48f_s^2 L_m^2} + \frac{n^2 \pi^2 I_H^2}{2}} \quad (27)$$

The root mean square value of the current  $I_{sw,rms\_L}$  which flows through switches at battery side can be expressed as equation (28).

$$I_{sw,rms\_L} = \sqrt{\frac{n^2 V_{Lm}^2}{96f_s^2 L_m^2} + \frac{\pi^2 I_H^2}{4n^2}} \quad (28)$$

The root-mean-square value of the current that flows through switches at battery side can be expressed as equation (29).

$$I_{DH,rms} = \frac{\pi}{2} I_H \quad (29)$$

The peak voltage across the resonant capacitor at battery side can be presented as equation (30).

$$V_{Cr2,pk} = \frac{\sqrt{2}I_{Lr2,rms}}{\omega C_{r1}} = \frac{\sqrt{\frac{n^2 V_{Lm}^2}{24f_s^2 L_m^2} + \frac{n^2 \pi^2 I_H^2}{4}}}{2\pi f_s C_{r2}} \quad (30)$$



From the equivalent circuit of the parasitic capacitors charging and discharging mode that shown in Fig. 11. To ensure the switches can operate in soft switching, the dead time of switching signal should meets requirements as equation (31). The dead time is 2% of switching time.

$$I_{Lm,pk} \cdot t_d \geq (C_{coss} + \frac{C_{coss} \cdot C_{coss}}{C_{coss} + C_{coss}}) \cdot \frac{V_H}{2} \quad (31)$$

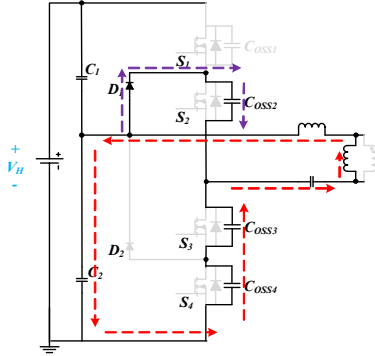


Fig. 11. The parasitic capacitors charging and discharging mode.

On the other hand, the value of magnetizing inductance influences the dead zone. Assume the dead zone is one percent of the operating period. The magnetizing inductance can be expressed as equation (32).

$$L_m \leq \frac{t_d T_s}{6 \cdot C_{coss}} \quad (32)$$

#### IV. EXPERIMENTAL RESULTS

The key parameters design is discussed in this chapter. The influence of quality factor  $Q$ , inductance ratio  $k$  and capacitance ratio  $m$  are analyzed with mathematical tool, MathCAD. The parameters of resonant tank can be derived from the variable  $Q$ ,  $k$  and  $m$ . Then, the value of voltages and currents are derived into equations from previous chapter. And the components can be selected depend on the calculation results. The specifications for the design of the bidirectional DC-DC converter can be found in TABLE II. For more detailed information about the parameters of the bidirectional DC-DC converter, please refer to TABLE III.

TABLE II. THE DESIGN SPECIFICATIONS OF THE BIDIRECTIONAL DC-DC CONVERTER

Specifications	Value
High voltage side voltage ( $V_H$ )	800 VDC
Battery side voltage ( $V_{Bat}$ )	200-400 VDC
Rated power (P)	1 kW
Resonant frequency	500 kHz
Switching Frequency ( $f_s$ )	350-850 kHz

TABLE III. PARAMETERS OF THE EXPERIMENTAL

Item	Symbol	Value
GaN-MOSFETs	$S_1 - S_8$	GS66508B
Three level side Capacitor	$C_1 - C_2$	14.4 $\mu$ F
Full bridge side Capacitor	$C_L$	40 $\mu$ F
Resonant Capacitor	$C_{r1}$ and $C_{r2}$	12.28 nF
Resonant Inductance	$L_{r1}$ and $L_{r2}$	8.2 $\mu$ H, 8.2 $\mu$ H
Magnetizing Inductance	$L_m$	17.4 $\mu$ H
Gate Driver IC		1EDF5673FXUMA1
Controller (DSP)		TMS320F28379D
Turns Ratio	$N$	1

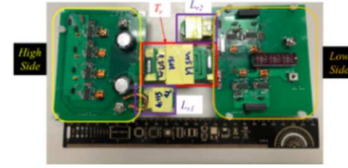


Fig. 12. The porpose circuit.

#### A. Experimental Waveforms of charging Mode

This condition  $V_{Bat}$  is 400 V at 500 kHz switching frequency. The experiment waveforms  $S_1$ ,  $S_2$ ,  $v_{cr1}$ ,  $i_{Lr1}$  are shown on Fig.13. Switch voltage of  $V_{ds1}$  and  $V_{ds2}$  can approach half of  $V_H$ . Waveforms of Switch voltage of  $V_{ds1}$  and  $V_{ds2}$  are equal to  $V_{Bat}$ .  $v_{cr2}$  and  $i_{Lr2}$  are shown on Fig. 14. From Fig. 15, the ZVS can be achieved.

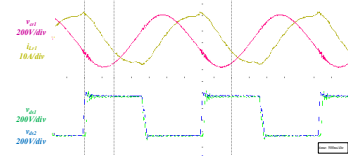


Fig. 13. The experiment results of three level half bridge side when  $V_{Bat}=400$  V,  $I_o=2.5$  A

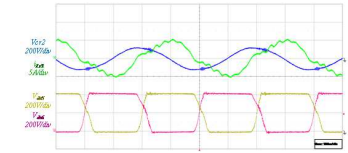


Fig. 14. The experiment results of full bridge side when  $V_{Bat}=400$  V,  $I_o=2.5$  A

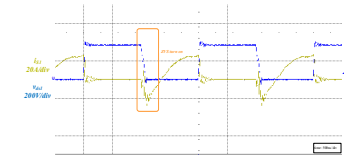


Fig. 15. The experiment results of ZVS.

### B. Experimental Waveforms of discharging Mode

The discharging condition when  $V_{\text{Bat}}$  is 400 V at 500 kHz switching frequency. The experiment waveforms  $S_5$ ,  $S_6$ ,  $v_{\text{cr}2}$ ,  $i_{\text{Lr}2}$  are shown on Fig. 16.  $S_1$ ,  $S_2$  and  $v_{\text{cr}1}$ ,  $i_{\text{Lr}1}$  are shown on Fig. 17. And the ZCS turn off waveform are shown on Fig. 18.

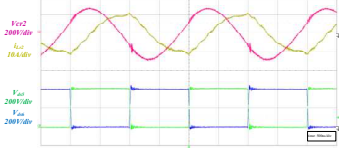


Fig. 16. The experiment results of full bridge side when  $V_{\text{Bat}}=400$  V,  $P_o=1$  kW.

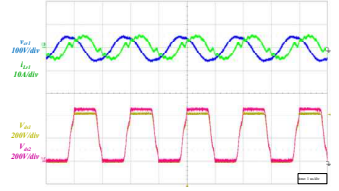


Fig. 17. The experiment results of three level half bridge side when  $V_{\text{Bat}}=400$  V,  $P_o=1$  kW.

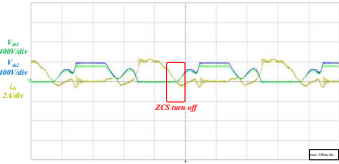


Fig. 18. The experiment results of ZCS

### C. Efficiency

The converter's efficiency is measure by Hioki 3390 power analyzer. On charging mode maximum efficiency is 94.2% as shown on Fig. 19 (a). And maximum efficiency on discharging mode is 93% as shown on Fig. 19 (b).

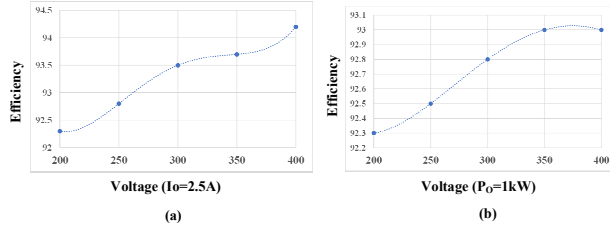


Fig. 19. (a)The efficiency on charging mode, (b)The efficiency on discharging mode.

### V. CONCLUSIONS

This study employs the diode-clamped three-level half-bridge configuration is utilized, which ensures that the voltage across each switch on the high-voltage side is maintained at half of  $V_H$ . Furthermore, the transfer of energy in two directions is enabled by the CLLC resonant tank in the converter. The rated power is 1 kW and the voltage on three level half bridge side is 800 V. The voltage on the battery side

is 200 V to 400 V. In addition, the high side switches can realize ZVS, and the battery side switches can realize ZCS, which reduces switching losses and improves efficiency. The maximum efficiency on charging mode achieved 94.2% and on discharging mode achieved 93%. The voltage of the GaN-MOSFETs does not exceed the rated voltage. From the analysis of the study circuit is analyzed, the specification of key parameters are deduced, This characteristic are verified from the simulation results and experimental results.

### ACKNOWLEDGMENT

The authors gratefully acknowledge financial support from the National Science and Technology Council of the Republic Of China (Taiwan) for financial support. Pursuant to grant number MOST 111-2221-E-006-078 and NSTC 112-2221-E-006-028.

### REFERENCES

- [1] P. He and A. Khaligh, "Comprehensive analyses and comparison of 1 kW isolated DC-DC converters for bidirectional EV charging systems," IEEE Transactions on Transportation Electrification, vol. 3, no. 1, pp. 147-156, 2016.
- [2] H. V. Nguyen and D. C. Lee, "Advanced single-phase onboard chargers with small DC-link capacitors," in 2018 IEEE International Power Electronics and Application Conference and Exposition (PEAC), 2018: IEEE, pp. 1-6.
- [3] T. Wickramasinghe, B. Allard, and N. Allali, "A review on single-phase, single-stage OBC topologies for EVs with 48 V powertrains," in IECON 2021-47th Annual Conference of the IEEE Industrial Electronics Society, 2021: IEEE, pp. 1-7.
- [4] S. Kim and F.S. Kang, "Multifunctional onboard battery charger for plug-in electric vehicles," IEEE Transactions on Industrial Electronics, vol. 62, no. 6, pp. 3460-3472, 2014.
- [5] H. Karneddi, D. Ronanki, and R. L. Fuentes, "Technological overview of onboard chargers for electrified automotive transportation," in IECON 2021-47th Annual Conference of the IEEE Industrial Electronics Society, 2021: IEEE, pp. 1-6.
- [6] M. Valente, T. Wijekoon, F. Freijedo, P. Pescetto, G. Pellegrino, and R. Bojoi, "Integrated on-board ev battery chargers: New perspectives and challenges for safety improvement," in 2021 IEEE Workshop on Electrical Machines Design, Control and Diagnosis (WEMDCD), 2021: IEEE, pp. 349-356.
- [7] J. Yuan, L. Dorn-Gomba, A. D. Callegaro, J. Reimers, and A. Emadi, "A review of bidirectional on-board chargers for electric vehicles," IEEE Access, vol. 9, pp. 51501-51518, 2021.
- [8] A. Sharma and R. Gupta, "Bharat DC001 Charging standard Based EV Fast Charger," in IECON 2020 The 46th Annual Conference of the IEEE Industrial Electronics Society, 2020: IEEE, pp. 3588-3593.
- [9] Z. U. Zahid, Z. M. Dalala, R. Chen, B. Chen, and J. Lai, "Design of bidirectional DC-DC resonant converter for vehicle-to-grid (V2G) applications," IEEE Trans. Transp. Electrific., vol. 1, no. 3, pp. 232-244, Oct. 2015, doi: 10.1109/TTE.2015.2476035.